Space-Doppler Adaptive Processing for Radar Imaging of Moving Targets masked by Ground Clutter

A. Bacci*†, M. Martorella*‡, D.A. Gray†, and F. Berizzi*‡ *Department of Information Engineering, University of Pisa, Italy
Email: alessio.bacci@for.unipi.it, [marco.martorella, fabrizio.berizzi] @iet.unipi.it
†University of Adelaide Radar Research Centre, EEE School, Australia
Email: dgray@eleceng.adelaide.edu.au ‡ Radar and Surveillance System (RaSS) National Laboratory,
National Inter-University Consortium for Telecommunications (CNIT), 56124 Pisa, Italy

Abstract

Non-cooperative moving targets appear defocussed within SAR images and, in the case of ground targets, the blurring effect due to the uncompensated target motion decreases the radar's detection capabilities. Ground clutter, if sufficiently strong, may also obscure individual scatterers on moving targets resulting in a decreased ability to successfully classify the target. In this work, clutter suppression and ISAR imaging are combined to obtain high resolution images of non-cooperative moving ground targets within SAR images. The clutter suppression technique proposed here is ISAR application oriented and is termed Space Doppler Adaptive Processing (SDAP). Results obtained by processing a real dataset demonstrate the effectiveness of the proposed method.

I. Introduction

Synthetic Aperture Radar (SAR) systems are a well known class of radars that exploit the relative motion between the radar platform and the target scene in order to obtain high resolution

images of large areas. Conventional SAR processing is based on the assumption that this motion is completely known and can be exploited in order to coherently process the received echoes. However non-cooperative moving targets in the scene are not focused and appear blurred and misplaced in the resulting SAR image [7]. On the other hand, ISAR processing is not reliant on a-priori knowledge of the relative radar-target motion, as this is estimated either before or while forming the synthetic aperture. In [21], ISAR processing has been demonstrated to be an effective tool for refocussing moving targets detected within SAR images. A detection step is also necessary before applying ISAR processing. In the case of slowly moving ground targets, strong ground clutter returns may partially of completely mask the target, making both detection and classification difficult.

Different techniques for the detection of moving targets can be found in the radar literature. The earliest method for discriminating moving target signals from static scene return in single channel SAR systems is based on differences in the Doppler spectra of stationary ground clutter and those of moving targets [10], [24]. This technique is based on the assumption that the radar PRF is high enough to obtain a region in the Doppler frequency domain that is free of the static scene components. Whilst the technique can readily be applied to single channel data, it suffers from some shortcomings. First of all, it requires a high PRF that results in both a reduction in the SAR swath width and an increase in the size of the block of data to be processed. Secondly, it generally fails when dealing with the detection of slow moving targets whose Doppler frequency falls completely within the Doppler bandwidth of the static scene. Other techniques proposed for detecting moving targets with single channel SAR systems are based on change detection algorithms which make use of different looks of the same scene at different times [32], or by the application of non-uniform sampling, i.e., non-uniform PRIs [18]. However, the effectiveness of all these methods when dealing with slow moving targets is limited in principle because the moving target returns cannot be separated from the static scene return in the Doppler domain.

More powerful methodologies to overcome these drawbacks are based on the use of more than one antenna to simultaneously collect different sets of data of the same scene. This capability of multiple spatial samples, i.e., echoes received from different antenna elements, and multiple time samples, i.e., echoes collected at different PRI intervals can be combined in order to obtain better performance in the presence of strong ground clutter. Along Track Interferometry (ATI)

[23][14][8], Displaced Phase Centre Array (DPCA) [11][29], Time-Frequency Transforms (TFT) [9][4][19] and Space Time Adaptive processing (STAP) are examples of the use of multichannel SAR systems for mitigating the deleterious effects of clutter. Specifically, STAP techniques are widely used for clutter mitigation purposes and have been widely treated for the general airborne radar case of slowly moving ground targets [17] [16] [30].

However in recent years, with the development of imaging systems with multichannel capabilities, researchers have studied the applicability of STAP processing in the multichannel radar imaging scenario. In [12], [13] optimum space-time processing for moving target detection in SAR was analytically derived, the implementation of slow-time STAP in both time and frequency domain was considered and a comparison between the optimal solution and a number of reduced rank methods carried out. The slow-time and frequency approaches are known as pre- and post-Doppler STAP respectively and in [27], [25] and [26] STAP processing of SAR data for jammer suppression was widely treated by considering both slow and fast time approaches.

In other studies, [4], a comprehensive investigation of combining STAP processing with a time-frequency analysis was carried out. This was done in order to obtain an estimation of the target instantaneous phase to be used for the successive formation of the synthetic aperture with respect to a detected moving target. In [33] a different approach that exploits multichannel information and is based on Velocity SAR (VSAR) is proposed. The processing scheme presented in such a paper is based on Velocity SAR (VSAR). It works pixel by pixel in the image domain to perform Moving Target Indication by exploiting only the spatial degrees of freedom (the number of channels).

Whilst STAP and its derivative approaches have been extensively investigated for suppressing clutter to allow the detection of slow moving ground targets its use for both clutter suppression and the imaging of moving targets have only recently been considered and in [2] a combination of STAP and ISAR techniques for the imaging of moving targets in SAR images has been proposed. The approach in [2] has been formulated in the space/slow-time domain and it can, as observed in [1], readily be extended the space Doppler domain. However, this aspect is not addressed in this paper.

In the work presented here an alternative to STAP and its various derivatives is proposed. The

new approach, originally presented in [3], is termed Space Doppler Adaptive Processing (SDAP) as its formulation is derived from a careful consideration of the Range Doppler (RD) image formation algorithm used in ISAR processing. This model is formulated in the Space/Doppler domain and, due to the RD specific features, is structurally and algorithmically different from STAP techniques implemented in the Doppler domain, i.e., the class of post-Doppler STAP algorithms discussed in [15].

This paper is organised as follows: the signal model is presented in Sect.II and it is used to derive the Multichannel Range Doppler (M-RD) algorithm and to analyse its limitation in Sect.III. Then, the SDAP ISAR processing is recalled in Sect.IV. Real data analysis is then used to prove the effectiveness of the presented algorithm. Results from this analysis are presented in Sect.V.

II. Signal Model

Let us consider the acquisition geometry in which a multichannel SAR with elements aligned along the flight path is mounted on an airborne platform and observes an area in which non-cooperative moving targets are present. The range compressed signal received at the pth, $p = -\frac{P}{2}, ..., \frac{P}{2} - 1$ antenna can be expressed as

$$S_p(f,t) = S_{t,p}(f,t) + S_{c,p}(f,t) + N_p(f,t) \tag{1}$$

where f is frequency (range frequency), t is slow time and $S_{t,p}(f,t)$, $S_{c,p}(f,t)$ and $N_p(f,t)$ are the target (moving), the clutter (stationary) and the noise contributions respectively. Under the assumption that the *straight iso range approximation* [6] holds true and the array size is much smaller than the radar target distance the received signal can be derived as follows.

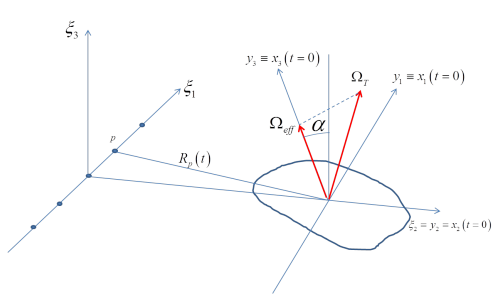

Figure 1. Multichannel ISAR geometry

The acquisition geometry is depicted in Fig.1 in which the centre of the reference system T_ξ is in the phase centre of the transmitter. The reference system T_ξ is oriented so that the axis ξ_2 is parallel to the radar LoS while ξ_1 is parallel to the array. The target motion can be expressed as the superimposition of the translational motion of the reference point, $R_0(t)$, and the rotational motion denoted by the rotation vector $\mathbf{\Omega}_T(t)$ applied to the reference point [6]. The projection of $\mathbf{\Omega}_T(t)$ on the plane orthogonal to the LoS is the effective rotation vector $\mathbf{\Omega}_{eff}(t)$. The reference system T_x has its origin on an arbitrary point on the target with the axis x_2 oriented along the LoS and the axis x_3 oriented along $\mathbf{\Omega}_{eff}(t)$. The reference system T_y is fixed on the target and coincides with T_x for $t = 0$. The angle α is the angle between ξ_3 and x_3. The received signal from the generic element p relative to the kth scatterer can be expressed as

$$S_{t,p}(f,t) = \sigma_k e^{j\frac{4\pi f}{c}\left[R_0^{(p)}(t)+\mathbf{y}^{(k)}\cdot\mathbf{i}_{LoS_y}^{(p)}(t)\right]} \tag{2}$$

where σ_k is the reflectivity of the kth scatterer located at $\mathbf{y}^{(k)}$ and $\mathbf{i}_{LoS_y}^{(p)}(t)$ is the LoS relative to the pth receiver expressed with respect to T_y.

As shown in [22] for small values of T_{obs} and, as a consequence of a constant rotation vector during the observation time ($\mathbf{\Omega}_T(t) \approx \mathbf{\Omega}_T$), the inner product in Eq.(2) can be expressed as follows (see details in Appendix A):

$$\mathbf{y}^{(k)} \cdot \mathbf{i}_{LoS_y}^{(p)}(t) = K_{0,k}^{(p)} + K_{1,k}^{(p)} t \tag{3}$$

where

$$\begin{aligned} K_{0,k}^{(p)} &= y_2^{(k)} - \tfrac{d}{R_0}\left[y_1^{(k)} p cos\left(\alpha\right) - y_3^{(k)} p \sin\left(\alpha\right)\right] \\ K_{1,k}^{(p)} &= c_2^{(k)} - \tfrac{d}{R_0}\left[c_1^{(k)} p cos\left(\alpha\right) - c_3^{(k)} p \sin\left(\alpha\right)\right] \end{aligned} \tag{4}$$

and where $c_1^{(k)}$, $c_2^{(k)} = \Omega_{eff} y_1^{(k)}$ and $c_3^{(k)}$ are the three components of the vector $\mathbf{c}^{(k)}$ defined in Eq.(40) of Appendix A.

The complex ISAR Point Spread Function (PSF) of the generic p^{th} channel relative to a single scatterer located at $\mathbf{y}^{(k)}$ can be obtained via the RD image formation algorithm applied to the motion compensated signal [6] and can be expressed as:

$$\begin{aligned} I^{(p)}(\tau,\nu) = BT_{obs}\sigma_k e^{j2\pi f_0\left(\tau-\frac{2}{c}K_{0,k}^{(p)}\right)} \times \\ \operatorname{sinc}\left[T_{obs}\left(\nu + \frac{2f_0}{c}K_{1,k}^{(p)}\right)\right] \operatorname{sinc}\left[B\left(\tau - \frac{2}{c}K_{0,k}^{(p)}\right)\right] \end{aligned} \tag{5}$$

where τ and ν denote the delay time and the Doppler frequency respectively.
After the scaling operation (from (τ, ν) to (y_1, y_2)) [6], Eq.5 can be approximated as:

$$\begin{aligned} I^{(p)}(y_1, y_2) =& BT_{obs}\sigma_k e^{j\frac{4\pi f_0}{c}(y_2 - K_{0,k}^{(p)})} \times \\ & \operatorname{sinc}\left[T_{obs}\left(y_1 + y_1^{(k)}\right)\right] \operatorname{sinc}\left[B\left(y_2 - y_2^{(k)}\right)\right] \end{aligned} \tag{6}$$

When using sampled data both the variables in the signal domain (f, t) and in the image domain (τ, ν) are discrete variables defined as:

$$\begin{array}{ll} f = f_0 + n\Delta_f & n = -\frac{N}{2}, ..., \frac{N}{2} - 1 \\ \tau = n_\tau \Delta_\tau & n_\tau = -\frac{N_\tau}{2}, ..., \frac{N_\tau}{2} - 1 \\ \nu = m_\nu \Delta_\nu & m_\nu = -\frac{M_\nu}{2}, ..., \frac{M_\nu}{2} - 1 \\ t = mT_R & m = -\frac{M}{2}, ..., \frac{M}{2} - 1 \end{array} . \tag{7}$$

Since the relationship between the frequency - slow time, (f, t), and the delay time - Doppler domain, (τ, ν), is given by a Fourier transform the sampling intervals can be expressed as follows:

$$\begin{array}{c} \Delta_\tau = \frac{1}{N\Delta_f} = \frac{1}{B} \\ \Delta_\nu = \frac{1}{MT_R} = \frac{1}{T_{obs}} \\ M_\nu = M \\ N_\tau = N \end{array} \tag{8}$$

The fully discrete signals are then defined as follows

$$S_p(n, m) \doteq S_p(f_0 + n\Delta f, mT_R) \tag{9}$$

$$I^{(p)}(n_\tau, m_\nu) \doteq I^{(p)}(n_\tau \Delta\tau, m_\nu \Delta\nu) \tag{10}$$

III. Multichannel Range Doppler

The Multichannel Range Doppler (M-RD) image is obtained by summing the P complex images obtained by processing the signals received by the P channels. It is worth pointing out that, since the focusing is performed with respect to a single point, the P images are aligned in phase only for this point. So, in order for points in the P images to be considered in phase throughout the whole of the imaging area under consideration, a bound for the phase difference among these points of the images must be evaluated which will determine the extent of the

sub-image that can be summed. This condition can be found by imposing an upper bound to the maximum phase difference among the images as follows:

$$\frac{4\pi}{\lambda}(P-1)\frac{d}{R_0}\left[y_1\cos(\alpha)-y_3\sin(\alpha)\right]\leq\frac{\pi}{8} \tag{11}$$

in which $\frac{\pi}{8}$ is reasonably chosen as the maximum phase difference allowed to consider all the contribution aligned in phase.

Such a bound leads to the following inequality:

$$D_{array}\leq\frac{\lambda R_0}{32\left[y_1\cos(\alpha)-y_3\sin(\alpha)\right]} \tag{12}$$

where $[y_1\cos(\alpha)-y_3\sin(\alpha)]$ is the target size in the ξ_1 dimension. It is quite clear that this condition depends on the array size and the target size along the direction parallel to the array. This method can still be applied when the target size along the ξ_1 dimension is larger than the bound expressed in Eq.(12), but in this case the whole region must be split into smaller regions (with dimension lower than the bound in Eq.(12)) and the focusing step must be applied to each of these regions separately. In order to better understand the distortions introduced when the requirement in Eq.(12) is not met, a closed form expression of the attenuation term can be evaluated. The resulting image can be expressed along the p channels

$$\begin{aligned} I_{M-RD}(y_1,y_2) &= \sum_{p=-\frac{P}{2}}^{\frac{P}{2}-1} I^{(p)}(y_1,y_2) \\ &= I^{(0)}(y_1,y_2)e^{+j\frac{4\pi}{\lambda}\frac{dPy_1}{2R_0}}\sum_{p=0}^{P-1}e^{j\frac{4\pi}{\lambda}\frac{d}{R_0}y_1p} \end{aligned} \tag{13}$$

The case in which $\alpha=0$ has been considered in order to simplify the notation. After some mathematical manipulations, Eq.(13) becomes

$$I_{M-RD}(y_1,y_2)=I^{(0)}(y_1,y_2)e^{j\frac{2\pi Pd}{\lambda 2R_0}y_1}\frac{\sin\left(\frac{2\pi dy_1P}{\lambda R_0}\right)}{\sin\left(\frac{2\pi dy_1}{\lambda R_0}\right)} \tag{14}$$

The term $J(y_1)=\frac{\sin\left(\frac{2\pi dy_1P}{\lambda R_0}\right)}{\sin\left(\frac{2\pi dy_1}{\lambda R_0}\right)}$ produces a distortion in the amplitude of the image due to the fact that for cross-range regions far away from the focusing point, the P images do not sum coherently as explained above.

The term $J(y_1)$ can be computed in order to evaluate the attenuation introduced by the incoherent summation along the channel dimension. It is worth noting that $J(y_1)$ can be neglected when both

the array size, i.e. $P \cdot d$, and the cross range offset from the focusing point, i.e. y_1, are sufficient small. These two conditions are usually verified in practical scenarios since the array size is limited by technological constraints and by the fact that long baselines, i.e., $d >> \frac{\lambda}{2}$, introduce a spatial subsampling that causes ambiguity in the beam domain, degrading the performance of SDAP and STAP filtering approaches. Moreover, the cross-range size of the imaging area is limited by the fact that the straight iso-range approximation must hold true to apply the proposed processing so that for high values of y_1 its applicability is limited in principle. In Fig.2 (a) and (c), the attenuation term $J(y_1)$ is shown for a radar centre-scene distance $R_0 = 5km$, a carrier frequency $f_0 = 10GHz$ and a baseline obtained by imposing the condition in Eq.(12) with $y_1 = 100m$ so that

$$d = \frac{\lambda R_0}{32 y_1 (P-1)} \tag{15}$$

It should be noted that for this example the condition in Eq.(12) is very restrictive, leading to a loss of $0.2dB$ within a distance of $100m$ from the focusing point in case of a ten element array (see Fig.2 (c)). The case in which the baseline is fixed at $d = \frac{\lambda}{2}$ is shown in Fig.2 (b) and (d), where the attenuation term for different values of P is represented. As can be noted this baseline value produces an acceptable loss of $0.5dB$ within a distance of $100m$ form the focusing point for a ten element array.

IV. Joint SDAP-ISAR

The joint SDAP-ISAR processing was first introduced in [3] and, for the sake of clarity, will be briefly reviewed here. Its difference with respect to the STAP-ISAR and its derivatives approaches discussed in [1] will be examined. Before delving into the mathematical details, it should be pointed out that the proposed SDAP processing is intimately linked to the RD image formation and the unusual formulation of the SDAP algorithm is a consequence of the RD approach being formulated in the range Doppler domain at the outset.

A. SDAP approach

Recalling the range slow-time signal model of Sect.II, the stacked multichannel signal (data) vector in the range Doppler domain can be written as

$$\tilde{\mathbf{S}}(n) = \left[\tilde{\mathbf{S}}(n,0), \tilde{\mathbf{S}}(n,1), ..., \tilde{\mathbf{S}}(n,M-1)\right]^T \in C^{MP \times 1} \tag{16}$$

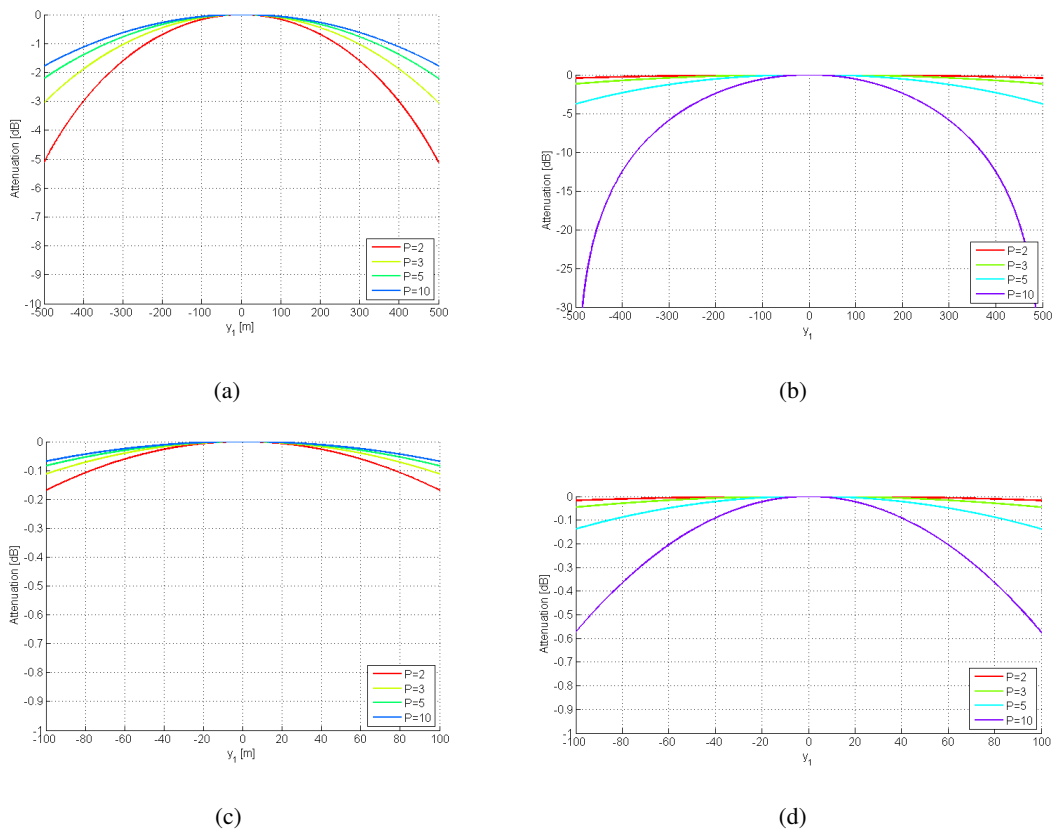

Figure 2. Attenuation factor: $d = \frac{\lambda R_0}{32 y_1 (P-1)}$ (a) $d = \frac{\lambda}{2}$ (b) $d = \frac{\lambda R_0}{32 y_1 (P-1)}$ zoom (c) $d = \frac{\lambda}{2}$ zoom (d)

where

$$\tilde{\mathbf{S}}(n, m_\nu) = \frac{1}{P} \left[\tilde{S}_1(n, m_\nu), \tilde{S}_2(n, m_\nu), ..., \tilde{S}_P(n, m_\nu) \right]^T \in C^{P \times 1} \tag{17}$$

$$\tilde{S}_p(n, m_\nu) = DFT_m \left\{ S_p(n, m) \right\} \tag{18}$$

and m_ν is the Doppler frequency index.

Again the Fourier transformation to the Doppler domain is pertinent to the RD imaging approach that follows the clutter mitigation step.

A reference vector for both conventional focussing or for optimum processing is similarly given by

$$\tilde{\mathbf{G}}_D(n, m_\nu) = \left[\tilde{\mathbf{S}}_{ref}(n, m_\nu), \tilde{\mathbf{S}}_{ref}(n, m_\nu - 1), ..., \tilde{\mathbf{S}}_{ref}(n, m_\nu - (M-1))\right]^T \in C^{MP\times 1} \tag{19}$$

where

$$\tilde{\mathbf{S}}_{ref}(n, m_\nu) = \frac{1}{P}\left[\tilde{S}_{ref,1}(n, m_\nu), \tilde{S}_{ref,2}(n, m_\nu), ..., \tilde{S}_{ref,P}(n, m_\nu)\right]^T \in C^{P\times 1} \tag{20}$$

and

$$\tilde{S}_{ref,p}(n, m_\nu) = DFT_m\left\{S_{ref,p}(n, m)\right\} \tag{21}$$

A key part of the conventional M-RD image formation processing incorporated here is the cross-range compression which is given by

$$u_D(n, m_\nu) = \tilde{\mathbf{G}}_D^H(n, m_\nu)\tilde{\mathbf{S}}(n) \tag{22}$$

It is worth pointing out that Eq.22 is the vectorial representation of the M-RD image formation processing described in Sect.III. This operation performs both cross-range compression at each channel via single channel RD and the summation of the P complex images as described above [3]. It is obvious then, that all the remarks about the phase term $K_0^{(p)}$ and the consequent distortion term $J(y_1)$ should be considered. In order to obtain an undistorted M-RD SAR image conditions allowing the distortion term to be neglected must be satisfied (as discussed in Sect.III).

The M-RD image formation described above can be generalised to an optimum filter, termed SDAP, by replacing the reference vector with the optimum weightvector, i.e.,

$$u_D(n, m_\nu) = \tilde{\mathbf{W}}_D^H(n, m_\nu)\tilde{\mathbf{S}}(n) \tag{23}$$

where the optimum filter is obtained by sample matrix inversion and is expressed as:

$$\tilde{\mathbf{W}}_D(n, m_\nu) = \gamma\hat{\mathbf{R}}_{Dc}^{-1}\tilde{\mathbf{G}}_D(n, m_\nu) \tag{24}$$

where γ is a scalar that does not affect the SINR at the output of the optimum filter and $\hat{\mathbf{R}}_{Dc}$ is an estimate of the interference cross-power spectral matrix $\mathbf{R}_{Dc}$. The latter is obtained by averaging along N_r target free range cells of training data, as analytically described in (25).

$$\hat{\mathbf{R}}_{Dc} = \frac{1}{N_r} \sum_{n_r=0}^{N_r-1} \tilde{\mathbf{Z}}(n_r)\tilde{\mathbf{Z}}^H(n_r) \in C^{MP\times MP} \tag{25}$$

The vector $\tilde{\mathbf{Z}}(n_r)$ denotes the target-free data in the nth range cell in the Space-Doppler domain. It is worth pointing out that the optimum processing in Eq.(23) performs both clutter suppression and image formation by means of the above mentioned M-RD processing. In order to obtain a well focused image of the non-cooperative moving target, the reference vector $\tilde{\mathbf{G}}_D(n, m_\nu)$ must compensate for both the platform and target own motion. Obviously, this is not a realistic situation since the target is non-cooperative. So, a first motion compensation is performed in the SDAP processing considering only the known part of the relative radar target motion while a high resolution image of a non-cooperative target is obtained by applying the ISAR processing at the SDAP output [3],[21].

B. Comparison with conventional STAP

In this section, the theoretical difference between the combined clutter suppression and cross-range compression of the SDAP approach and the clutter cancellation of the post-Doppler STAP approach, [1], are examined. Only the case of cross-range compression processing, i.e., in which the clutter covariance matrix is diagonal, is considered as it simply demonstrates the difference. The generalization to non-diagonal matrices is straightforward.

By recalling Eq.(22) and by writing the cross-range compressed SDAP output in component form we obtain:

$$u_D\left(n, m_\nu\right) = \sum_k \tilde{\mathbf{S}}_{ref}^H\left(n, m_\nu - k\right) \tilde{\mathbf{S}}\left(n, k\right) \tag{26}$$

The range slow time output of the STAP algorithm is given by [2]

$$f(n, m) = \sum_k \mathbf{S}_{ref}^H(n, m-k)\mathbf{S}(n, k) = \mathbf{G}^H(n, m)\mathbf{S}(n) \tag{27}$$

where $\mathbf{G}(n,m)$ and $\mathbf{S}(n)$ are the reference vector and the signal vector in the space slow time domain [2].

The post-Doppler STAP formulation is obtained by applying the unitary transformation $\mathbf{T}$ defined in [1], [17] and [15] as follows

$$f(n,m) = \tilde{\mathbf{G}}^H(n,m_\nu)\tilde{\mathbf{S}}(n) \tag{28}$$

where $\tilde{\mathbf{G}}(n,m_\nu) = \mathbf{T}\mathbf{G}(n,m)$. It is evident that $\tilde{\mathbf{G}}(n,m_\nu)$ in the post-Doppler STAP and $\mathbf{G}_D(n,m_\nu)$ (Eq.19) in the proposed SDAP are defined in two different ways which makes SDAP and post-Doppler STAP approaches fundamentally different. Another way to appreciate the difference between STAP and SDAP consists on transforming both sides of Eq.(27) to the Doppler frequency domain as follows

$$F(n,m_\nu) = FT_m\left\{f(n,m)\right\} = \tilde{\mathbf{S}}^H_{ref}(n,m_\nu)\tilde{\mathbf{S}}(n,m_\nu) \tag{29}$$

resulting in a significantly different expression to that of Eq.(26).

C. Sub-optimum SDAP

A sub-optimum processing scheme is described in [3] which allows for the reduction of the amount of training data needed to estimate the cross-power spectral matrix. In this approach the Doppler spectrum is split into adjacent frequency bands of length L and the SDAP is carried out by using only the L Doppler bins within each band.

The functional block is depicted in Fig.3 and is expressed as shown in (30)

$$u_{D,i}(n,m_\nu) = \tilde{\mathbf{W}}^H_{D,i}(n,m_\nu)\tilde{\mathbf{S}}_i(n) \tag{30}$$

where $\tilde{\mathbf{W}}_{D,i}(n,m_\nu)$ and $\tilde{\mathbf{S}}_i(n)$ are the weightvector and the signal vector relatively to the ith block. The weightvector in the ith window is expressed as:

$$\tilde{\mathbf{W}}_{D,i}(n,m_\nu) = \hat{\mathbf{R}}^{-1}_{Dc,i}\tilde{\mathbf{G}}_{D,i}(n,m_\nu) \tag{31}$$

where $\tilde{\mathbf{G}}_{D,i}(n,m_\nu)$, $\tilde{\mathbf{S}}_i\left(n\right)$ and $\hat{\mathbf{R}}_{Dc,i}$ are defined as follows [3].

$$\tilde{\mathbf{G}}_{D,i}(n,m_\nu) = \begin{bmatrix} \tilde{\mathbf{S}}_{ref}\left(n, m_\nu - (i-1)L\right) \\ \tilde{\mathbf{S}}_{ref}\left(n, m_\nu - ((i-1)L+1)\right) \\ \tilde{\mathbf{S}}_{ref}\left(n, m_\nu - ((i-1)L+2)\right) \\ \vdots \\ \tilde{\mathbf{S}}_{ref}\left(n, m_\nu - (iL-1)\right) \end{bmatrix} \in C^{LP\times 1} \tag{32}$$

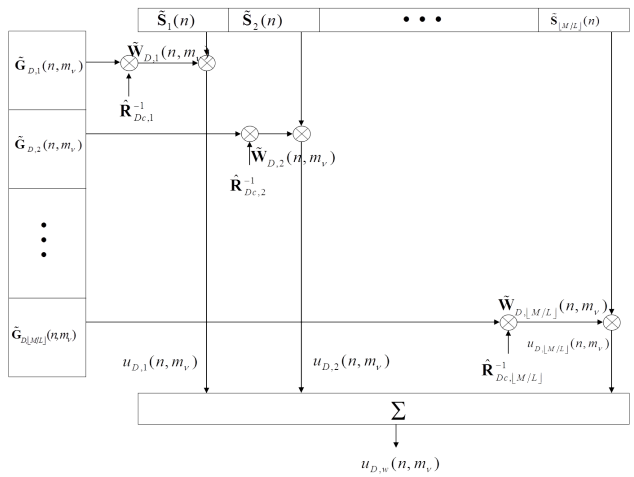

Figure 3. Sub-optimum SDAP-ISAR functional block

and

$$\tilde{\mathbf{S}}_i(n) = \begin{bmatrix} \tilde{\mathbf{S}}(n,(i-1)L) \\ \tilde{\mathbf{S}}(n,(i-1)L+1) \\ \tilde{\mathbf{S}}(n,(i-1)L+2) \\ \vdots \\ \tilde{\mathbf{S}}(n,iL-1) \end{bmatrix} \in C^{LP\times 1} \tag{33}$$

The estimate of cross-power spectral matrix in the ith window, $\hat{\mathbf{R}}_{Dc,i}$, is obtained as

$$\hat{\mathbf{R}}_{Dc,i} = \frac{1}{N_r}\sum_{n_r=0}^{N_r-1} \tilde{\mathbf{Z}}_i(n_r)\tilde{\mathbf{Z}}_i^H(n_r) \in C^{LP\times LP} \tag{34}$$

where $\tilde{\mathbf{Z}}_i(n_r)$ denotes the target-free data in the n_r range cell relative to the ith window. The global output of the sub-optimum SDAP filtering process is

$$u_{D,w}(n,m_\nu) = \sum_i u_{D,i}(n,m_\nu) \tag{35}$$

As illustrated in the above equation and in Fig.3 the final output is the coherent summation of each of the clutter filtered subsets. The windowing operation performed in this sub-optimum SDAP results in an approximation of the cross-power spectral matrix used for clutter suppression. Since the windows are then all coherently processed, there is no loss of information from the

imaging point of view. In fact, if no clutter suppression is considered, i.e. $\hat{\mathbf{R}}_{Dc,i} = \mathbf{I}$ the sub optimum and the optimum approaches are exactly equivalent.

D. Remarks on the proposed approach

It is worth pointing out that, as stated before, the proposed clutter suppression algorithm relies on the applicability of the RD image formation algorithm, which depends on some defined assumptions. Specifically, small values of T_{obs} ($\mathbf{\Omega}_{eff}$ not varying with time) and a radar-target distance much larger than the target's size (straight iso-range approximation) must be ensured. In the case in which the above mentioned hypothesis do not hold true, different algorithms based on temporal matched filter should be used to form the SAR image and to suppress the static clutter [2]. It is also worth pointing out that the RD is not the best image formation algorithm to obtain SAR images since algorithms based on temporal matched filter provide better resolved SAR images. Nevertheless, the aim of this processing is providing high resolution ISAR images of non-cooperative moving targets and in this case the RD is a viable approach. Moreover, since the clutter suppressed images of each target must be back projected onto the data domain before applying ISAR processing [21], using the RD to form the clutter suppressed image allows for an exact and easy inversion via the 2D-IFT of the crop containing the target of interest.

V. Experimental Results

The proposed processing was tested on real data provided by Metasensing[1] acquired using a two-channel SAR system. The acquisition has been performed by flying over a highway in the proximity of Teuge airport. The highway was perpendicular to the flight trajectory. The acquisition parameters are summarized in Tab.I. The radar parameters are listed in Tab.II. It is quite obvious that the experimental parameters described are not optimal for testing the proposed method. The principal shortcomings are

- Small bandwidth ($B = 120MHz$). This involves a slant-range resolution $\Delta_{y_2} = 1.25m$ which is a relatively poor resolution especially when dealing with small ground targets.
- Baseline $d > \frac{\lambda}{2}$. This is a problem from both a beamforming and M-RD image formation point of view.

[1] www.metasensing.com

Platform	208 Grand Caravan from Paracentrum Teuge (PH-SWP)
Look angle	$55°$
Flight Altitude	$1200m$
Velocity	$180km/h$
Mean Range	$2km$
Swath	$1km$

Table I

ACQUISITION PARAMETERS

Center Frequency	$9.6GHz$
TX Bandwidth	$120MHz$
PRF	$5kHz$
ADC sampling frequency	25MHz
TX: horn	
Gain	$19.6dB$
Antenna Aperture ($3dB$)	elevation $20°$ azimuth $20°$
RX: microstrip patch	
Gain	$21.4dB$
Antenna Aperture ($3dB$)	elevation $22°$ azimuth $7.5°$
Baseline	$15cm$

Table II

RADAR PARAMETERS

- Only two channels, resulting in a small number of spatial degrees of freedom.
- Highway parallel to the range dimension. This make estimation of the interference space/slow time covariance matrix difficult.

In order to reduce the baseline between the 2 antennas, the first N_d samples are discarded from channel 1 and the last N_d samples are discarded from channel 2 data (this operation is depicted in Fig.4 (a)). In this way the equivalent baseline, d_{eq}, becomes

$$d_{eq} = d - N_d v_p T_R \tag{36}$$

It is quite obvious that in this case, the acquisitions are no longer simultaneous. Since the SAR

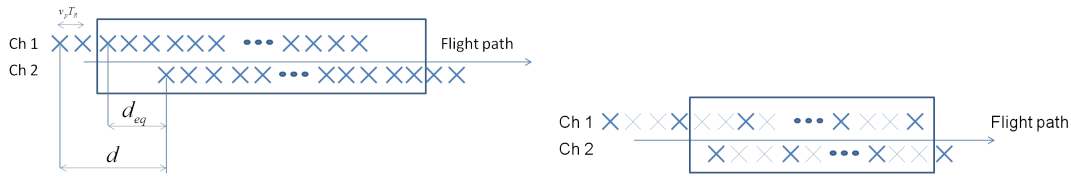

(a) (b)

Figure 4. Baseline reduction (a) baseline reduction and subsampling (b)

transmitter is coherent this is not an issue for image formation processing but can affect the radar performance in terms of suppressing non-stationary ground clutter.

A. *Imaging results*

As it has been explained in the Sect.IV, the conditions in Eq.12 must be met. This allows the P images, obtained by processing the data collected by the P different channels, to sum in phase. In this way little distortion is introduced by the multichannel imaging processing.

It is worth pointing out that, Eq.(12) imposes a direct relationship between the image cross-range and the array size since in a SAR scenario $\alpha = 0$ (see Fig.1).

The available data are acquired by a multichannel SAR system with two channels and an inter-element distance $d = 15cm \approx 5\lambda$. Such a distance does not meet the condition in Eq.(12) given the values of cross-range, y_1, imaging area and the array size, D_{array}. In fact, considering the system parameters listed in Tab.II, the cross range imaging size can be roughly evaluated by considering the receiver antenna beamwidth and can be expressed as follows

$$D_{y_1} \approx R_0 \theta_{az} = 262m \tag{37}$$

The results in terms of images obtained by applying the conventional single channel RD algorithm to channel 1 and channel 2 are shown in Fig.5 (a) and (b) respectively. The image obtained by applying M-RD without discarding any data, i.e. $N_d = 0$, is shown in Fig.6 (a). The distortions due to the above mentioned effects are evident. The array size is too large and the two images sum in phase only in a small cross-range region.

Results with different values of discarded data, N_d, are shown in Fig.6 (b)-(e). Considering the system parameters described above ($d = 15cm$, $v_p = 45m/s$, $PRF = 5kHz$) and Eq.(36), the configuration in which the equivalent baseline is minimized is with $N_d = 17$.

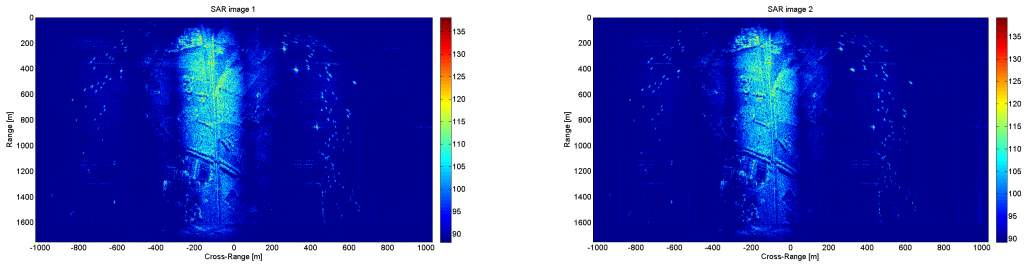

(a) (b)

Figure 5. RD image results (a) channel 1, (b) channel 2

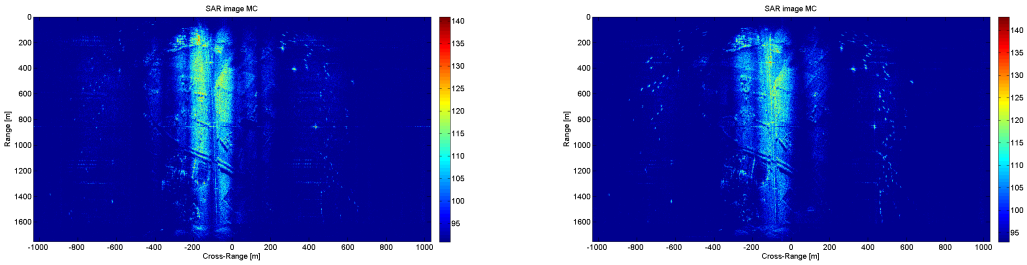

(a) (b)

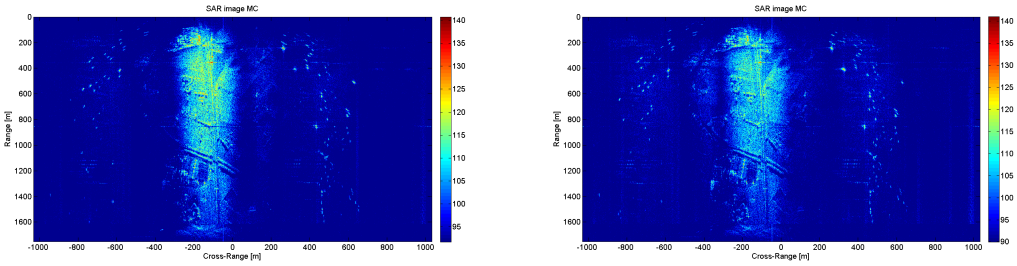

(c) (d)

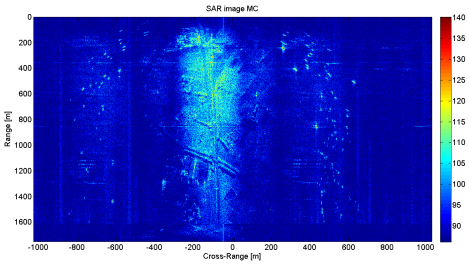

(e)

Figure 6. M-RD image results (a) $N_d = 0$, (b) $N_d = 7$, (c) $N_d = 12$, (d) $N_d = 15$, (e) $N_d = 17$

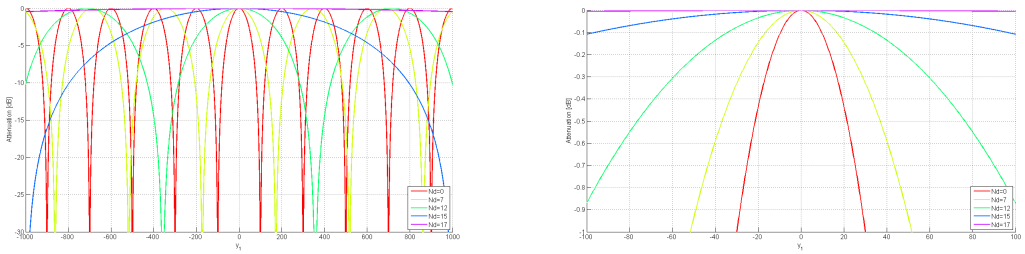

(a) (b)

Figure 7. Attenuation term with respect to N_d

It is evident by observing Fig.6 that the closer the antenna elements are, the larger the undistorted image region is, as predicted in Sect.II. The attenuation term is depicted in Fig.7 for different values of N_d.

B. Clutter suppression and imaging results

In Fig.6 (e), it is apparent that a lot of moving targets are present outside the clutter Doppler bandwidth. In order to better evaluate the effectiveness of the proposed processing a case in which some targets are present in the clutter Doppler bandwidth will be considered. This can easily be obtained by performing a sub-sampling in the slow time dimension (in addition to the baseline reduction) as shown in Fig.4(b).

A subsampling factor of 3 has been chosen resulting in an equivalent PRF equal to $PRF_{eq} = \frac{PRF}{3} = 1.67kHz$. A results of this subsampling is that certain targets will be aliased into the bandwidth of the clutter spectrum and the fixed relationship between the Doppler frequency of a target in the image obtained considering the data without subsampling and the Doppler frequency of the same target in the image obtained by processing the data with PRF_{eq} exists and can be exploited in order to verify if some moving targets are cancelled by the clutter suppression process. Specifically, a target with Doppler frequency $|f_D| < \frac{PRF_{eq}}{2}$ will appear in the same Doppler position within the images obtained by processing the data with the two PRF values. On the other hand, targets whose Doppler frequency $\frac{PRF_{eq}}{2} < |f_D| < \frac{PRF}{2}$ will be wrapped in the image obtained by processing the data with PRF_{eq}. In this way, a pseudo ground truth is created and can be used to verify the effectiveness of the proposed algorithm. Moreover, the subsampling operation involves a reduction of the data to be processed. This allows for the processing of

larger Coherent Processing Intervals (CPIs) of data without increasing the computation time. It is quite obvious that the larger the CPI of data processed is the finer the image resolution in the Cross-Range (Doppler) dimension is.

The SAR image obtained by processing the subsampled data is shown in Fig.8 (a). The region under test and the training range cells are in the red and the yellow boxes respectively.

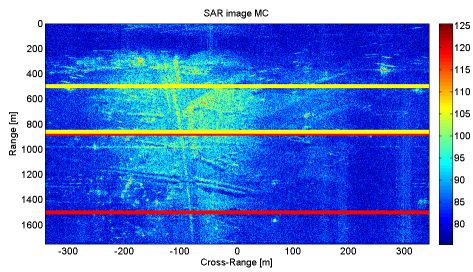

(a)

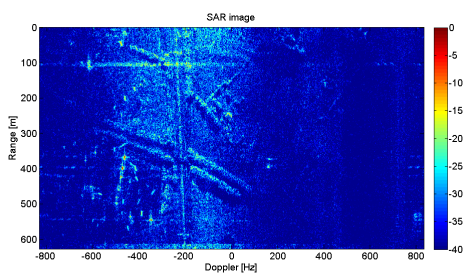

(b)

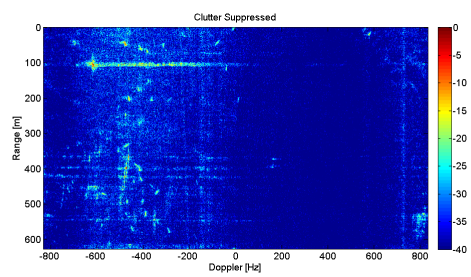

(c)

Figure 8. SAR image obtained processing subsampled data (a) region under test (b) region under test clutter suppressed (c)

The SAR images of the region under test without clutter suppression and with clutter suppression are shown in Fig.8 (b) and (c) respectively.[2] It is quite evident that, in this case, some of the targets that in Fig.6 are outside the clutter Doppler bandwidth are aliased into the band occupied by clutter and so masked by the ground return. This is due to the subsampling process as explained before. Moreover, as can be noted by a visual inspection, clutter suppression seems to work effectively as a lot of targets that are masked in Fig.8 (b) become clearly visible in Fig.8 (c).

In order to better appreciate the improvement in the moving target detection capability in

[2]It is worth pointing out that in all the following figures the $range = 0m$ corresponds to the beginning of the region under test.

Fig.9,11 and 13, three sub-regions are shown without the application of the clutter mitigation processing (a) and with the application of the clutter mitigation processing (b). Moreover, the portions of the image obtained by processing the data without subsampling, $PRF = 5kHz$, in which the same targets are present are shown in Fig.9,11 and 13 (c). These last three images represent the Doppler region, that in the image obtained by processing the subsampled data, are folded within the clutter Doppler bandwidth. As a consequence, they provide the pseudo ground truth that can be exploited in order to verify the effectiveness of the proposed method.

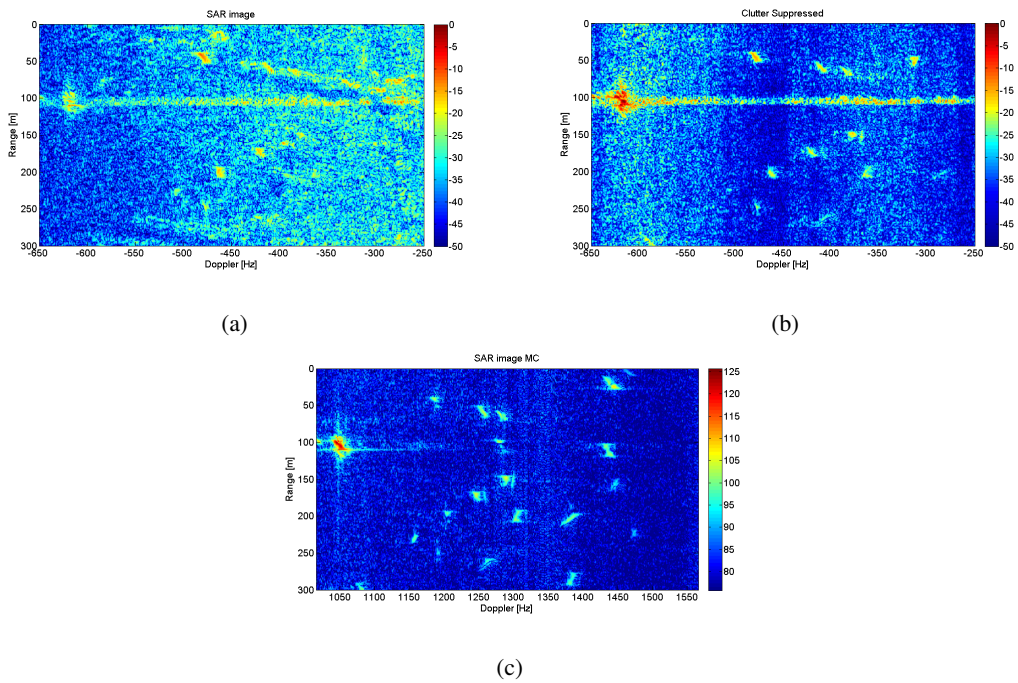

Figure 9. Sub-region 1: SAR image (a) Clutter suppressed SAR image (b) Pseudo ground truth (c)

The Doppler frequencies of every visible target in the pseudo ground truth images (Fig.9,11 and 13 (c)) are listed in Tab.III,V and VII respectively with the relative Doppler frequency evaluated by considering the sub-sampling operation. The range coordinates are also listed in order to locate the target in Fig.9,11 and 13 (b) and (c). It should be noted that four targets out of twenty-seven are cancelled in the three considered sub-regions.

It is worth pointing out that the target that can be clearly seen in Fig.9 (b) with coordinates range and Doppler coordinates, $Range = 55m$ and $f_D = -310Hz$ respectively, does not appear in Fig.9 (c). This is not an artefact introduced by the processing but corresponds to a target at a range of $55m$ and $f_D = -1976Hz$ in the $5kHz$ data that folds into the area under test. (Note

Target N.	f_D [Hz]	$f_{D_{eq}}$ [Hz]	Range [m]	Missing targets
1	1187	-479	40	
2	1257	-409	58	
3	1284	-382	65	
4	1047	-619	103	
5	1288	-378	147	
6	1250	-416	172	
7	1203	-463	197	
8	1305	-361	199	
9	1383	-283	204	X
10	1158	-504	227	X

Table III

SUB-REGION 1: PSEUDO GROUND TRUTH COMPARISON

this target is barely visible in Fig.6 (e) but when this figure is expanded becomes visible)

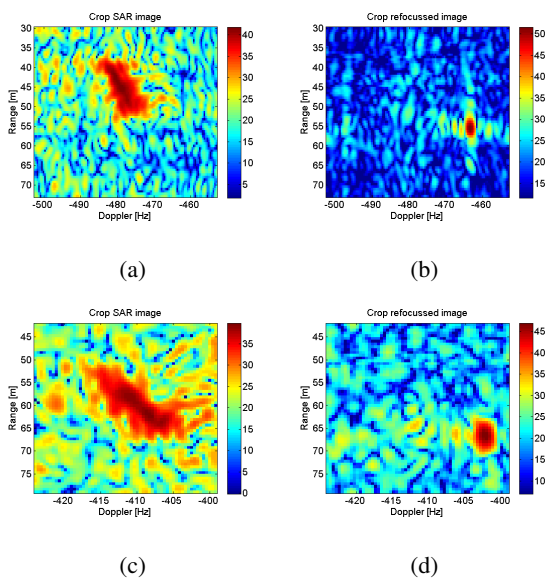

Figure 10. Sub-region 1 - Crop 1: original SAR image (a) refocussed image (b);Crop 2: original SAR image (c) refocussed image (d)

In Fig.10, Fig.12 and Fig.14 the results of the application of the ISAR processing [21] are shown. Specifically, 6 targets were selected (Target n. 1,2 from the sub-region 1 and Target n.2,4 from sub-region 2 and Target n.1,4 from sub-image 3) and for each of them the SAR image (a)

and (c) and the refocussed ISAR image (b) and (d) are shown. In order to better evaluate the performance of the refocussing process the image contrast (IC) [20] values before and after the autofocusing are listed in Tab.IV, VI and VIII for all the targets detected in Fig.9, 11 and 13 (b). It is worth pointing out that, the blank spaces correspond to the few targets on which the ISAR refocusing processing fails because either the clutter is not well cancelled the filtering destroys the target return as well. Although the targets are too small compared to the system resolution the improvement in the image quality is evident in terms of energy concentration.

Target N.	**IC SAR**	**IC ISAR**
1	2.673	10.174
2	1.472	4.84
3	0.83	3.344
4	2.80	5.326
5	1.345	3.698
6	1.161	4.165
7	1.879	6.502
8	1.072	4.92

Table IV

SUB-REGION 1: IC VALUES BEFORE AND AFTER ISAR PROCESSING

Target N.	f_D [Hz]	f_D [Hz]	Range [m]	Missing targets
1	-1674	-7	3	
2	-1750	-85	43	
3	-1708	-43	122	
4	-1655	-12	205	

Table V

SUB-REGION 2: PSEUDO GROUND TRUTH COMPARISON

VI. CONCLUSION

ISAR processing has been demonstrated to be an effective tool in obtaining well focused high resolution images of moving targets within SAR images. In strong clutter environments, detection can be a critical step because of the spreading of the useful target energy due to the

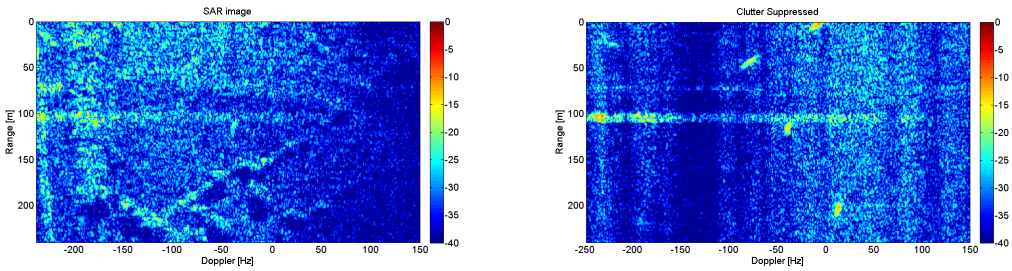

(a) (b)

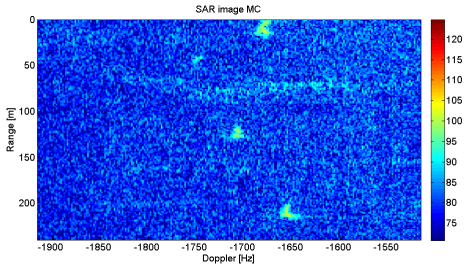

(c)

Figure 11. Sub-region 2: SAR image (a) Clutter suppressed SAR image (b) Pseudo ground truth (c)

Target N.	IC SAR	IC ISAR
1	2.105	5.805
2	2.343	6.728
3		
4	1.915	5.087

Table VI

SUB-REGION 2: IC VALUES BEFORE AND AFTER ISAR PROCESSING

uncompensated target own motion. A combined SDAP ISAR processing has been proposed to address this problem by performing both adaptive filtering to mitigate against clutter and ISAR imaging to focus moving target returns. Results obtained by applying this technique to real data have demonstrated its effectiveness. Future work will aim at testing the SDAP-ISAR effectiveness with either higher resolution radars and similar targets or larger targets with similar resolution and comparing the STAP and the SDAP approaches. The results in these cases should then emphasise the benefits obtainable with the proposed processing in terms of target classification/recognition.

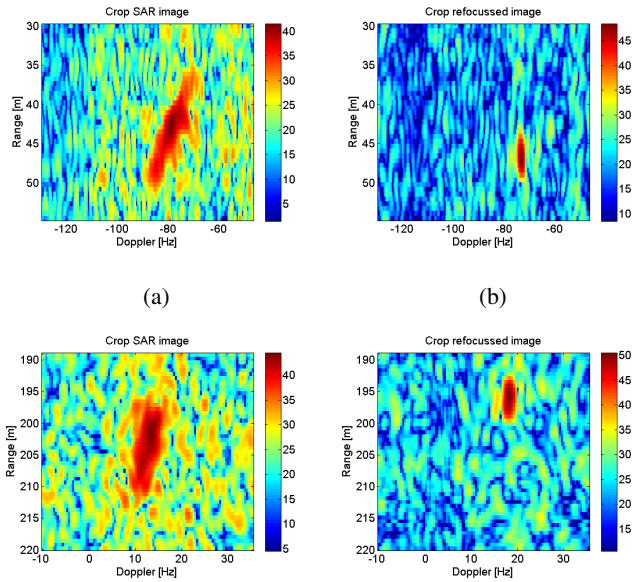

(a) (b)

(c) (d)

Figure 12. Sub-region 2 - Crop 4: original SAR image (a) refocussed image (b); Crop 6: original SAR image (c) refocussed image (d)

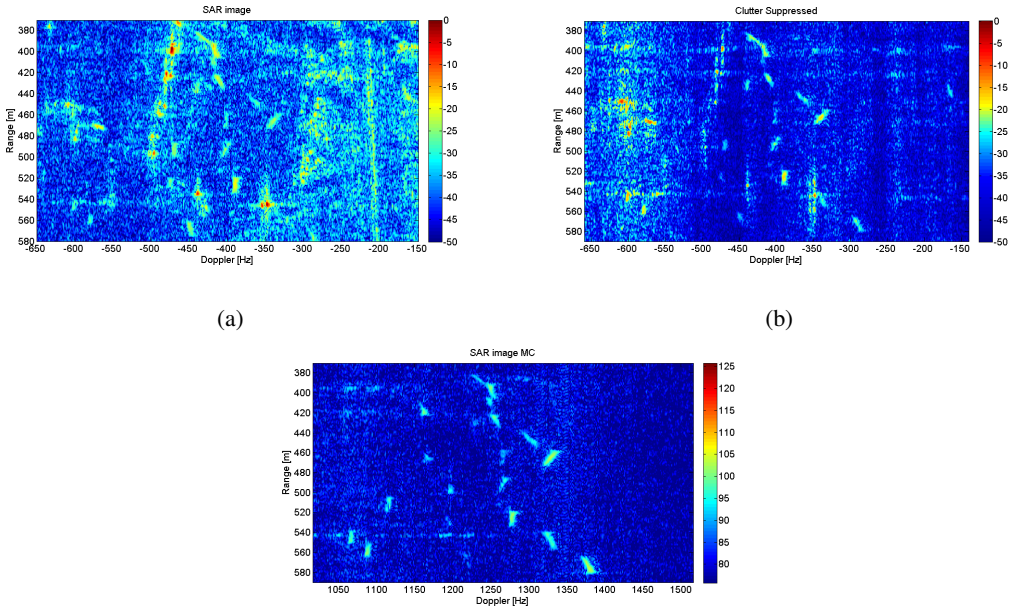

(a) (b)

(c)

Figure 13. Sub-region 3: SAR image (a) Clutter suppressed SAR image (b) Pseudo ground truth (c)

Target N.	f_D [Hz]	$f_{D_{eq}}$ [Hz]	Range [m]	Missing targets
1	1255	-412	395	
2	1165	-502	419	X
3	1257	-410	427	
4	1301	-366	445	
5	1332	-355	465	
6	1268	-399	489	
7	1198	-469	498	
8	1117	-550	510	
9	1281	-386	524	
10	1667	-600	543	X
11	1329	-338	546	
12	1090	-577	558	
13	1379	-288	573	

Table VII

SUB-REGION 3: PSEUDO GROUND TRUTH COMPARISON

Target N.	**IC SAR**	**IC ISAR**
1	1.475	4.935
3	1.812	5.560
4		
5	1.856	7.673
6	1.455	4.694
7	1.028	3.703
9	1.615	6.327
10		
11		
12	0.882	2.755
13	1.426	5.774

Table VIII

SUB-REGION 3: IC VALUES BEFORE AND AFTER ISAR PROCESSING

ACKNOWLEDGMENT

The authors would like to thank Metasensing for providing the real dataset used in this paper. Part of this work has been carried out within the activities of the NATO-SET 196 on on

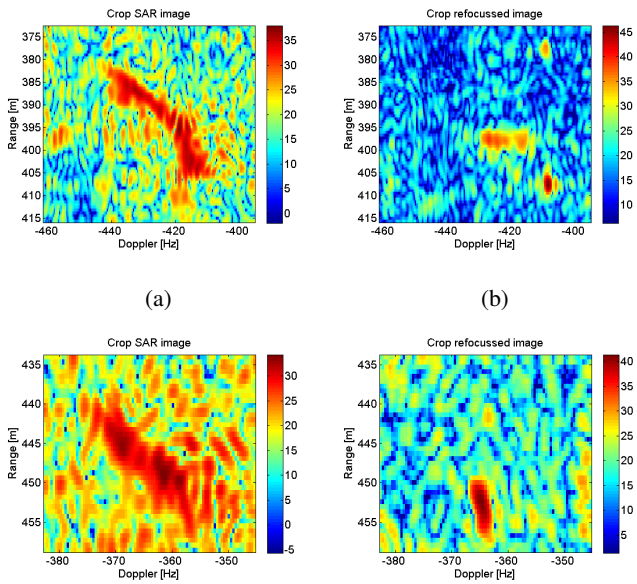

Figure 14. Sub-image 3 - Crop 1: original SAR image (a) refocussed image (b); Crop 4: original SAR image (c) refocussed image (d)

Multchannel/Multistatic Radar Imaging of Non-Cooperative Targets.

APPENDIX A

SIGNAL MODELING

In this appendix mathematical details to derive Eq.3 are given.

As shown in [22] the inner product in Eq.(2) can be expressed with respect the T_x reference system as follows:

$$\mathbf{y}^{(k)} \cdot \mathbf{i}^{(p)}_{LoS_y}(t) = \mathbf{x}^{(k)}(t) \cdot \mathbf{i}^{(p)}_{LoS_x}(t) \tag{38}$$

Under the assumption of a small T_{obs} the total rotation vector can be considered as constant, i.e., $\mathbf{\Omega}_T(t) \approx \mathbf{\Omega}_T$ and the image plane fixed with respect to T_ξ. As a consequence, the position of the target's point scatterer $\mathbf{x}^{(k)}(t)$ can be calculated by solving the following differential equation system:

$$\begin{cases} \dot{\mathbf{x}}^{(k)}(t) = \mathbf{\Omega}_T \times \mathbf{x}^{(k)}(t) \\ \mathbf{x}^{(k)}(0) = \mathbf{y}^{(k)} \end{cases} \tag{39}$$

The resulting closed form solution is expressed as follows [5], [6], [28]

$$\mathbf{x}^{(k)}(t) = \mathbf{a}^{(k)} + \mathbf{b}^{(k)}\cos(\Omega t) + \frac{\mathbf{c}^{(k)}}{\Omega}\sin(\Omega t) \tag{40}$$

where $\mathbf{a}^{(k)} = \frac{\mathbf{\Omega}_T \cdot \mathbf{y}^{(k)}}{\Omega^2}\mathbf{\Omega}_T$, $\mathbf{b}^{(k)} = \mathbf{y}^{(k)} - \frac{\mathbf{\Omega}_T \cdot \mathbf{y}^{(k)}}{\Omega^2}\mathbf{\Omega}_T$, $\mathbf{c}^{(k)} = \mathbf{\Omega}_T \times \mathbf{y}^{(k)}$ and $\Omega = |\mathbf{\Omega}_T|$.

For small T_{obs} Eq.(40) can be approximated by its first-order Taylor series around $t = 0$ and the results is expressed as follows:

$$\mathbf{x}^{(k)}(t) = \mathbf{a}^{(k)} + \mathbf{b}^{(k)} + \mathbf{c}^{(k)}t \tag{41}$$

This approximation means that the Doppler frequency of each scatterer is constant and then the ISAR image can be obtained by the RD technique [31], [20].

By considering the matrix $\mathbf{M}_{\xi\mathbf{x}}$ which describes the rotation of the reference system T_x of an angle α with respect T_ξ as defined as follows

$$\mathbf{M}_{\xi\mathbf{x}} = \begin{bmatrix} \cos(\alpha) & 0 & \sin(\alpha) \\ 0 & 1 & 0 \\ -\sin(\alpha) & 0 & \cos(\alpha) \end{bmatrix} \tag{42}$$

the LoS unit vectors $\mathbf{i}^{(p)}_{LoS_x}(t)$ can be expressed as the normalized distance between the position of each sensor and the origin of T_x:

$$\mathbf{i}^{(p)}_{LoS_x}(t) = \begin{bmatrix} \frac{-pdcos(\alpha)}{\sqrt{R_0^2(t)+(pd)^2}} & \frac{R_0(t)}{R_0^2(t)+(pd)^2} & \frac{pd\sin(\alpha)}{\sqrt{R_0^2(t)+(pd)^2}} \end{bmatrix}^T \tag{43}$$

By substituting Eq.43 and by approximating $R_0(t) \approx R_0(0) = R_0$ (reasonable for small observation time) and the terms $\sqrt{R_0^2(t) + (pd)^2} \approx R_0$ (reasonable for short baselines) the inner product in Eq.(38) can be expressed as follows:

$$\mathbf{y}^{(k)} \cdot \mathbf{i}^{(p)}_{LoS_y}(t) = K^{(p)}_{0,k} + K^{(p)}_{1,k}t \tag{44}$$

where

$$\begin{aligned} K^{(p)}_{0,k} &= y^{(k)}_2 - \tfrac{d}{R_0}\left[y^{(k)}_1 pcos(\alpha) - y^{(k)}_3 p\sin(\alpha)\right] \\ K^{(p)}_{1,k} &= c^{(k)}_2 - \tfrac{d}{R_0}\left[c^{(k)}_1 pcos(\alpha) - c^{(k)}_3 p\sin(\alpha)\right] \end{aligned} \tag{45}$$

and where $c^{(k)}_1$, $c^{(k)}_2 = \Omega_{eff} y^{(k)}_1$ and $c^{(k)}_3$ are the three components of the vector $\mathbf{c}^{(k)}$ defined in Eq.(40).

REFERENCES

[1] BACCI, A. *Optimal Space Time Adaptive Processing for Multichannel Inverse Synthetic Aperture Radar Imaging*. PhD thesis, University of Pisa, Italy & University of Adelaide, Australia, May 2014.

[2] BACCI, A., GRAY, D., MARTORELLA, M., AND BERIZZI, F. Joint STAP-ISAR for non-cooperative target imaging in strong clutter. In *Radar Conference (RADAR), 2013 IEEE* (2013), pp. 1–5.

[3] BACCI, A., GRAY, D., MARTORELLA, M., AND BERIZZI, F. Space-doppler processing for multichannel isar imaging of non-cooperative targets embedded in strong clutter. In *Radar (Radar), 2013 International Conference on* (2013), pp. 43–47.

[4] BARBAROSSA, S., AND FARINA, A. Space-time-frequency processing of synthetic aperture radar signals. *Aerospace and Electronic Systems, IEEE Transactions on 30*, 2 (1994), 341–358.

[5] BATTISTI, N., AND MARTORELLA, M. Intereferometric phase and target motion estimation for accurate 3d reflectivity reconstruction in isar systems. In *Radar Conference, 2010 IEEE* (May 2010), pp. 108–112.

[6] BERIZZI, F., MESE, E., DIANI, M., AND MARTORELLA, M. High-resolution isar imaging of maneuvering targets by means of the range instantaneous doppler technique: modeling and performance analysis. *Image Processing, IEEE Transactions on 10*, 12 (2001), 1880–1890.

[7] CARRARA, W., GOODMAN, R., AND MAJEWSKI, R. *Spotlight Synthetic Aperture Radar: Signal Processing Algorithms*. Artech House signal processing library. Artech House, Incorporated, 1995.

[8] CHAPIN, E., AND CHEN, C. Along-track interferometry for ground moving target indication. *Aerospace and Electronic Systems Magazine, IEEE 23*, 6 (2008), 19–24.

[9] COHEN, L. Time-frequency distributions-a review. *Proceedings of the IEEE 77*, 7 (1989), 941–981.

[10] D'ADDIO, E., BISCEGLIE, M. D., AND BOTTALICO, S. Detection of moving objects with airborne {SAR}. *Signal Processing 36*, 2 (1994), 149 – 162.

[11] DICKEY, F.R., J., LABITT, M., AND STAUDAHER, F. Development of airborne moving target radar for long range surveillance. *Aerospace and Electronic Systems, IEEE Transactions on 27*, 6 (1991), 959–972.

[12] ENDER, J. Space-time adaptive processing for synthetic aperture radar. In *Space-Time Adaptive Processing (Ref. No. 1998/241), IEE Colloquium on* (apr 1998), pp. 6/1 –618.

[13] ENDER, J. H. G. Space-time processing for multichannel synthetic aperture radar. *Electronics Communication Engineering Journal 11*, 1 (1999), 29–38.

[14] GIERULL, C. Moving target detection by along-track sar interferometry. In *DREO Technical Report* (2002).

[15] GREVE, S., RIES, P., LAPIERRE, F., AND VERLY, J. Framework and taxonomy for radar space-time adaptive processing (stap) methods. *Aerospace and Electronic Systems, IEEE Transactions on 43*, 3 (July 2007), 1084–1099.

[16] GUERCI, J. *Space-time Adaptive Processing for Radar*. Artech House radar library. Artech House, 2003.

[17] KLEMM, R., OF ENGINEERING, I., AND TECHNOLOGY. *Principles of Space-Time Adaptive Processing, 3rd Edition*. IET radar, sonar, navigation and avionics series. Institution of Engineering and Technology, 2006.

[18] LEGG, J. A., BOLTON, A. G., AND GRAY, D. A. Sar moving target detection using a non-uniform prf. In *European SAR conference* (1996), pp. 423–426.

[19] LOMBARDO, P. Estimation of target motion parameters from dual-channel sar echoes via time-frequency analysis. In *Radar Conference, 1997., IEEE National* (1997), pp. 13–18.

[20] MARTORELLA, M., BERIZZI, F., AND HAYWOOD, B. Contrast maximisation based technique for 2-d isar autofocusing. *Radar, Sonar and Navigation, IEE Proceedings - 152*, 4 (2005), 253–262.

[21] MARTORELLA, M., GIUSTI, E., BERIZZI, F., BACCI, A., AND DALLE MESE, E. Isar based techniques for refocusing non-cooperative targets in sar images. *Radar, Sonar Navigation, IET 6*, 5 (2012), 332–340.

[22] MARTORELLA, M., SALVETTI, F., AND STAGLIANO, D. 3d target reconstruction by means of 2d-isar imaging and interferometry. In *Radar Conference (RADAR), 2013 IEEE* (2013), pp. 1–6.

[23] PASCAZIO, V., SCHIRINZI, G., AND FARINA, A. Moving target detection by along-track interferometry. In *Geoscience and Remote Sensing Symposium, 2001. IGARSS '01. IEEE 2001 International* (2001), vol. 7, pp. 3024–3026 vol.7.

[24] RANEY, R. Synthetic aperture imaging radar and moving targets. *Aerospace and Electronic Systems, IEEE Transactions on AES-7*, 3 (1971), 499–505.

[25] ROSENBERG, L., AND GRAY, D. Robust interference suppression for multichannel sar. In *Signal Processing and Its Applications, 2005. Proceedings of the Eighth International Symposium on* (28-31, 2005), vol. 2, pp. 883 – 886.

[26] ROSENBERG, L., AND GRAY, D. Anti-jamming techniques for multichannel sar imaging. *Radar, Sonar and Navigation, IEE Proceedings - 153*, 3 (june 2006), 234 – 242.

[27] ROSENBERG, L., TRINKLE, M., AND GRAY, D. Fast-time stap performance in pre and post range processing adaption as applied to multichannel sar. In *Radar Symposium, 2006. IRS 2006. International* (may 2006), pp. 1 –4.

[28] SCAGLIONE, A., AND BARBAROSSA, S. Estimating motion parameters using parametric modeling based on time-frequency representations. In *Radar 97 (Conf. Publ. No. 449)* (Oct 1997), pp. 280–284.

[29] SKOLNIK, M. *Radar Handbook, Third Edition*. Electronics electrical engineering. McGraw-Hill Education, 2008.

[30] WARD, J. *Space-Time Adaptive Processing for Airborne Radar*. Massachusset Inst of Tech Lexinton Lincoln Lab, 1994.

[31] WEHNER, D. *High-Resolution Radar*. Radar Library. Artech House, Incorporated, 1995.

[32] WHITE, R. Change detection in sar imagery. In *Synthetic Aperture Radar, IEE Colloquium on* (1989), pp. 5/1–5/3.

[33] XU, J., LI, G., PENG, Y.-N., XIA, X.-G., AND WANG, Y.-L. Parametric velocity synthetic aperture radar:signal modeling and optimal methods. *Geoscience and Remote Sensing, IEEE Transactions on 46*, 9 (Sept 2008), 2463–2480.